Journal of Materials Science & Technology 108 (2022) 256–269

Contents lists available at ScienceDirect

Journal of Materials Science & Technology

journal homepage: www.elsevier.com/locate/jmst

Research Article

Mechanical property comparisons between CrCoNi medium-entropy alloy and 316 stainless steels

Xiaoru Liu[a,b,1], Hao Feng[c,1], Jing Wang[a,1], Xuefei Chen[a,b], Ping Jiang[a], Fuping Yuan[a,b], Huabing Li[c,*], En Ma[d,*], Xiaolei Wu[a,b,*]

[a] State Key Laboratory of Nonlinear Mechanics, Institute of Mechanics, Chinese Academy of Sciences, Beijing 100190, China
[b] School of Engineering Science, University of Chinese Academy of Sciences, Beijing 100049, China
[c] School of Metallurgy, Northeastern University, Shenyang 110819, China
[d] Center for Alloy Innovation and Design (CAID), State Key Laboratory for Mechanical Behavior of Materials, Xi'an Jiaotong University, Xi'an 710049, China

ARTICLE INFO

Article history:
Received 19 July 2021
Revised 17 August 2021
Accepted 18 August 2021
Available online 31 October 2021

Keywords:
Medium-entropy alloy
Austenite stainless steel
Strain hardening
Ductility
Fracture toughness
Charpy impact toughness

ABSTRACT

We systematically compared the mechanical properties of CrCoNi, a recently emerged prototypical medium-entropy alloy (MEA) with face-centered-cubic (FCC) structure, with hallmark FCC alloys, in particular, the well-known austenitic 316L and 316LN stainless steels, which are also concentrated single-phase FCC solid solutions and arguably next-of-kin to the MEAs. The tensile and impact properties, across the temperatures range from 373 K to 4.2 K, as well as fracture toughness at 298 K and 77 K, were documented. From room temperature to cryogenic temperature, all three alloys exhibited similarly good mechanical properties; CrCoNi increased its tensile uniform elongation and fracture toughness, which was different from the decreasing trend of the 316L and 316LN. On the other hand, the stainless steels showed higher fracture toughness than CrCoNi at all temperatures. To explain the differences in macroscopic mechanical properties of the three alloys, microstructural hardening mechanisms were surveyed. CrCoNi MEA relied on abundant mechanical twinning on the nanoscale, while martensitic transformation was dominant in 316L at low temperatures. The deformation mechanisms in the plastic zone ahead of the propagating crack in impact and fracture toughness tests were also analyzed and compared for the three alloys.

1. Introduction

Over the past several years, a large number of high-entropy alloys (HEAs) and medium-entropy alloys (MEAs) have been developed [1–7], many of which are solid solutions with face-centered cubic (FCC) structure. These H/MEAs are equi-atomic or near-equimolar multi-component alloys with three or more elements [1–9]. Due to the unusual multi-principal element composition, H/MEAs have been claimed to possess superior mechanical properties [10–23]. Among the single-phase FCC H/MEAs, CrCoNi MEA has higher strength and ductility than most FCC HEAs [9,24,25], although the CrCoNi MEA is composed of only three principal elements. The fracture toughness properties of CrCoNi are even better than those of the original five-component NiCrCoFeMn HEAs (Cantor alloys) [12,18], which makes CrCoNi a representative multi-principal element alloy. However, commercial austenitic stainless steels (ss) and cryogenic alloys such as MP35N [26], which are widely used for example as reactor pressure vessels, also display good mechanical properties at both elevated and cryogenic temperatures [26–31]. Interestingly, they are also single-phase FCC solid solutions (concentrated in Fe-Cr-Ni) with similar low stacking fault energy (SFE) as FCC H/MEAs. But direct comparisons of FCC H/MEAs with commercial austenitic stainless steels have rarely been studied.

Specifically, two issues arise on the difference between the CrCoNi MEA and austenitic stainless steels. Firstly, how does CrCoNi MEA compare with austenitic stainless steels such as the familiar 316L and 316LN, in terms of mechanical properties at various temperatures, from tensile stress-strain behavior to fracture toughness? Secondly, when the CrCoNi MEA performs differently from FCC stainless steels, what is the reason for the different work-hardening mechanisms? To answer these questions, we investigated the tensile, impact, and fracture toughness properties of CrCoNi MEA in a shoulder-to-shoulder comparison with the two representative types of austenitic stainless steels (316L and 316LN).

* Corresponding authors.
E-mail addresses: lihb@smm.neu.edu.cn (H. Li), maen@xjtu.edu.cn (E. Ma), xlwu@imech.ac.cn (X. Wu).
[1] These authors contributed equally to this work.

https://doi.org/10.1016/j.jmst.2021.08.057
1005-0302/

Table 1
Chemical compositions of CrCoNi, 316L and 316LN.

Material	Chemical composition (at.%)												
	N	C	Cr	Ni	Co	Mn	Mo	Si	S	P	O	Al	Fe
CrCoNi			33.4	33.3	33.3								
316L	0.024	0.07	17.99	12.31	–	1.86	1.48	0.80	0.0060	0.012	0.0038	0.11	Bal.
316LN	0.67	0.065	18.42	11.75	–	1.83	1.40	0.69	0.0056	0.013	0.0035	0.11	Bal.

Tensile and impact testing were performed at 373–4.2 K, and fracture toughness tests were performed at 298 K and 77 K. The microstructures were characterized to explain the mechanical behavior under various conditions.

2. Materials, processing, and testing methods

2.1. Materials and processing

The chemical compositions of the three alloys used in this work are listed in Table 1. CrCoNi is equi-atomic in Cr, Co and Ni, while 316L and 316LN are concentrated in Fe, Cr and Ni, and 316LN has much higher concentration of nitrogen compared with 316L. The ternary equi-atomic CrCoNi ingot was produced from high-purity (>99.9%) elements, which was electromagnetically levitated and melted under argon atmosphere and then drop-casted into rectangular ingot with the size of 70 mm × 70 mm × 110 mm. The ingot was then homogenized in vacuum at 1473 K for 12 h and then forged at 873–923 K, followed by annealing at 1173 K for 2 h. The 316L and 316LN were manufactured using a vacuum induction furnace. The ingots were kept at 1453 K for 40 min, and then hot forged at 1323–1453 K into 30 mm thick plates. The plates were subsequently annealed at 1323 K for 0.5 h for 316L and 2 h for 316LN, respectively, followed by water-quenching. For fracture toughness testing, the plate of 316LN was cold-rolled to 13 mm, with a thickness reduction of 55%, and then annealed at 1173 K for 0.5 h.

2.2. Testing methods of mechanical properties

The flat specimens for tensile testing were all obtained *via* electrical discharge machining (EDM) from recrystallized sheets of CrCoNi MEA, 316L and 316LN ss. The specimen shape was dog-bone, with a gage section of 4 mm × 1 mm and a length of 15 mm. The quasi-static tensile tests were conducted at a strain rate of 5×10^{-4} s^{-1} at 373–4.2 K using an MTS Landmark servo-hydraulic testing machine equipped with a remodeled environmental chamber.

The standard full-size Charpy V-notch (CVN) impact specimen was processed, with the size of 10 mm × 10 mm × 55 mm and the V-notch of a radius of 0.25±0.025 mm. The direction of V-notch was paralleled to the transverse direction (TD). The impact testing was performed at 373–4.2 K. For tests at 373–77 K, an NCS NI750C instrumented Charpy pendulum impact tester of 750 J capacity (NCS Testing Technology Co., LTD), equipped with an instrumented Charpy impulse data acquisition system, was used, according to the ASTM E23 standard [32]. For liquid-helium temperature (LHT) tests at 4.2 K, an MTS PTMS4750 pendulum impact tester was employed.

For fracture toughness tests, compact-tension (C(T)) specimens were processed with a thickness (B) of 10 mm, and a width (W) of 20 mm. A straight-through notch was cut with a length of 9 mm according to ASTM standard E1820 [33]. Fatigue pre-cracking was made in force control with a stress ratio (R) of 0.1, using an MTS Landmark servo-hydraulic testing machine at room temperature (RT). The length of the final pre-crack was between 15 and 20 mm. After that, side grooves were machined on both surfaces with a total thickness reduction of 0.1W to ensure a straight and sharp crack front. The fracture toughness testing was performed on an SANS universal testing machine equipped with a cryogenic environmental chamber at a constant displacement loading rate of 0.5 mm/min at RT and liquid nitrogen temperature (LNT), and the load-line displacement (LLD) was detected using an Epsilon clip gauge. The crack extension size and J-integral were obtained from the LLD curves, using the elastic compliance method. Fracture toughness testing was not conducted on CrCoNi, for which data are available in Ref. [18].

Vickers micro-hardness (HV) distributions (hardness contours) around the crack tip for the impact and fracture toughness tested samples were examined with a Future-Tech ARS900 Vickers microhardness tester used a load of 25 gf and a dwell time of 15 s on the polished crack surfaces (normal direction, ND). The hardness indentation sites along the radius direction are separated by a distance of 0.1–0.5 mm from one another.

2.3. Microstructure characterization

The phase compositions, prior to testing and after tensile and impact testing of CrCoNi, 316L and 316LN at 298, 77 and 4.2 K were examined using X-ray diffraction (XRD) with the Cu-$K\alpha$ radiation at 40 kV and 40 mA on 1.0-mm-thick slices. The XRD scans cover the 2θ range from 20° to 100°, with a step size of 0.01° and a dwell time of 2 s each step.

Microstructural features were investigated using a Zeiss GeminiSEM 300 scanning electron microscope (SEM) equipped with an electron backscatter diffraction (EBSD) system from Oxford. The fracture morphologies after impact and fracture toughness testing were observed using a secondary electron detector in a Zeiss Supra 55 field emission SEM at 15 kV.

The deformation microstructure was also examined using a transmission electron microscope (TEM, JEOL JSM-2100F) operated at 200 kV. Thin foils for TEM observation were cut from the gauge sections of the tensile samples, ground to about 40 μm thick and finally thinned *via* twin-jet polishing using a solution of 8% perchloric acid and 92% ethanol at −25°C with a potential of 38 V.

3. Experimental results

3.1. Microstructure characterization

Fig. 1 summarizes the microstructures after full recrystallization annealing in all three alloys of CrCoNi, 316L, and 316LN, respectively. As expected, all EBSD images show a single-phase FCC structure of equiaxed grains, as shown in Fig. 1(a–f). Of special note is the presence of multi-modal grain size distribution in all three alloys, see Fig. 1(g). To be specific, two size peaks are easily discernable at 10 μm and 50 μm, respectively, in CrCoNi. Several peaks are visible in 316LN. Smaller grains usually distribute at the grain boundaries (GBs) and triple junctions of larger grains. The average grain sizes in CrCoNi, 316L, and 316LN are 26, 31, and 92 μm, respectively. The average grain sizes of CrCoNi and 316L are similar, whereas that of 316LN is much larger. Furthermore, Σ3 twin

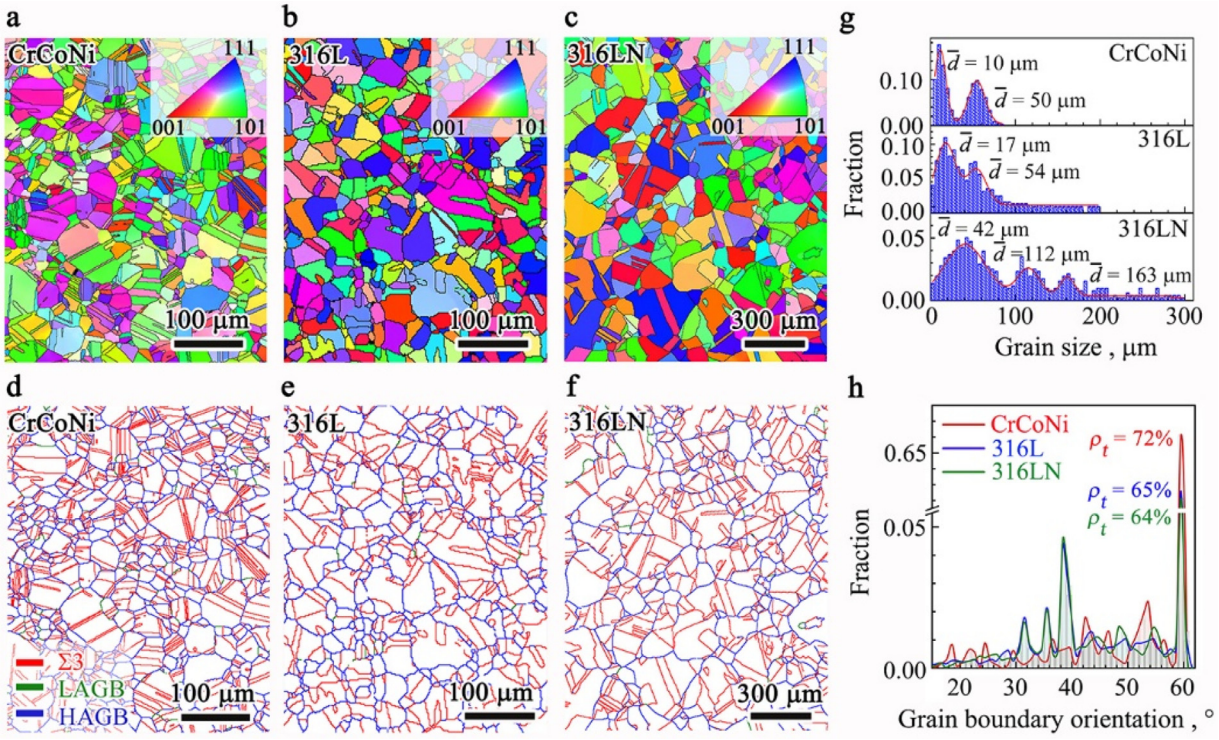

Fig. 1. EBSD images showing the hetero-structure after recrystallization annealing in CrCoNi, 316L, and 316LN, respectively. (a–c) Inverse pole figure (IPF) images of the three alloys. All are equi-axed grains of complete recrystallization. (d–f) Grain boundary (GB) images of the three alloys. Σ3: twin boundary. LAGB: low-angle GB of misorientation ranging from 5° to 15°. HAGB: high-angle GB of misorientation ≥15°. (g) and (h) Distribution of both grain size and grain boundary orientation in the three alloys. Note the size distribution of bi-modal in both CrCoNi and 316L and multi-modal in 316LN, respectively. ρ_t: density of annealing twins.

boundaries (TBs) are dominant, see Fig. 1(h). This is the result of the low stacking fault energy (SFE) in these three alloys. The volume fraction (ρ_t) of TBs is 72%, 65%, and 64% for CrCoNi, 316L, and 316LN, respectively. Distinctly, CrCoNi has a higher density of annealing twins than 316L and 316LN.

3.2. Mechanical properties

3.2.1. Tensile properties

Fig. 2 displays the quasi-static tensile behaviors in CrCoNi, 316L, and 316LN. Fig. 2(a–c) are the engineering stress–strain ($\sigma_e - \varepsilon_e$) curves at three typical applied temperatures (T) of 298, 77 and 4.2 K. The corresponding strain hardening rates ($^{\partial\sigma}/_{\partial\varepsilon}$) normalized by flow stress (σ_f) are shown as a function of true strain, see Fig. 2(d–f). All ($\sigma_e - \varepsilon_e$) curves at temperatures between 373 K and 4.2 K are shown in Fig. S1 in Supplementary Materials. The yield strength (σ_y) is higher in both CrCoNi and 316LN than that in 316L at 298 K, see Fig. 2(a). This is expected because both Cr and Ni in CrCoNi are principal elements, rather than solutes of fairly high concentration (Table 1). The increased lattice distortion caused by multiple principal components and their interactions with moving dislocations effectively impede the motion of dislocation in CrCoNi, providing solid solution (cocktail) hardening [8–10]. The grain size is also smaller in MEA, see Fig. 1(g). In addition, nitrogen, an interstitial atom in 316LN, enhances the strength to make up for the reduced carbon content in the solid solution [34,35]. The elongation-to-failure and strain hardening rates are not very different. At 77 K (Fig. 2(b)) and 4.2 K (Fig. 2(c)), σ_y increases for all the three alloys, as expected. Interestingly, CrCoNi still shows an increased uniform elongation (ε_u), compared with 316L and 316LN with a slightly decreased ε_u, relative to that at 298 K. In addition, serrated flow is observed at 4.2 K for all three alloys, which was reported before in $Al_{0.5}CoCrCuFeNi$ [36] and 316L stainless steel [37], and attributed to the dynamic strain ageing. This interpretation is controversial but beyond the scope of this article.

The normalized strain hardening rate shows a monotonic decrease at 298 K in all three alloys, see Fig. 2(d). At 77 K and 4.2 K, however, 316L and 316LN display a two-stage hardening behavior, different from the monotonous decrease of strain hardening rate with strain in CrCoNi. In the first stage, the hardening rate rapidly decreases both in 316L and 316LN. In the second stage, the hardening rate shows an obvious up-turn at strain ranging from 10% to 25% in 316L, and a much slower drop under higher strain (true strain is greater than 20%) in 316LN. The characteristic of two-stage hardening at low temperatures in austenitic stainless steels is usually ascribed to the stress-induced martensitic phase transformation [38,39].

Fig. 2(g) shows the change of both σ_y and ε_u at varying testing T ranging from 373 K to 4.2 K in CrCoNi, 316L, and 316LN. Two main results are seen. First, σ_y rises with the drop of T in three alloys; 316LN shows the fastest rise in σ_y. Second, ε_u in CrCoNi shows a monotonic rise as T decreases. In other words, CrCoNi shows a simultaneous rise in both σ_y and ε_u as T drops, well in line with the previous result in CrCoNi and other single-phase FCC HEAs [9,23,24]. By contrast, ε_u rises at first and drops later in both 316L and 316LN, and ε_u drops much earlier in 316L than in 316LN.

Fig. 2(h) shows the (σ_y, ε_u) balance in the three alloys. Comparing the CrCoNi with 316L and 316LN, a synergistic increase of both σ_y and ε_u can be seen when the temperature drops, while a trade-off between σ_y and ε_u occurs in 316L and 316LN, when the temperature drops to 253 K and 173 K, respectively. Therefore, CrCoNi has the best combination of strength and plasticity at varying temperatures, and that of 316LN is the next in line, followed by 316L.

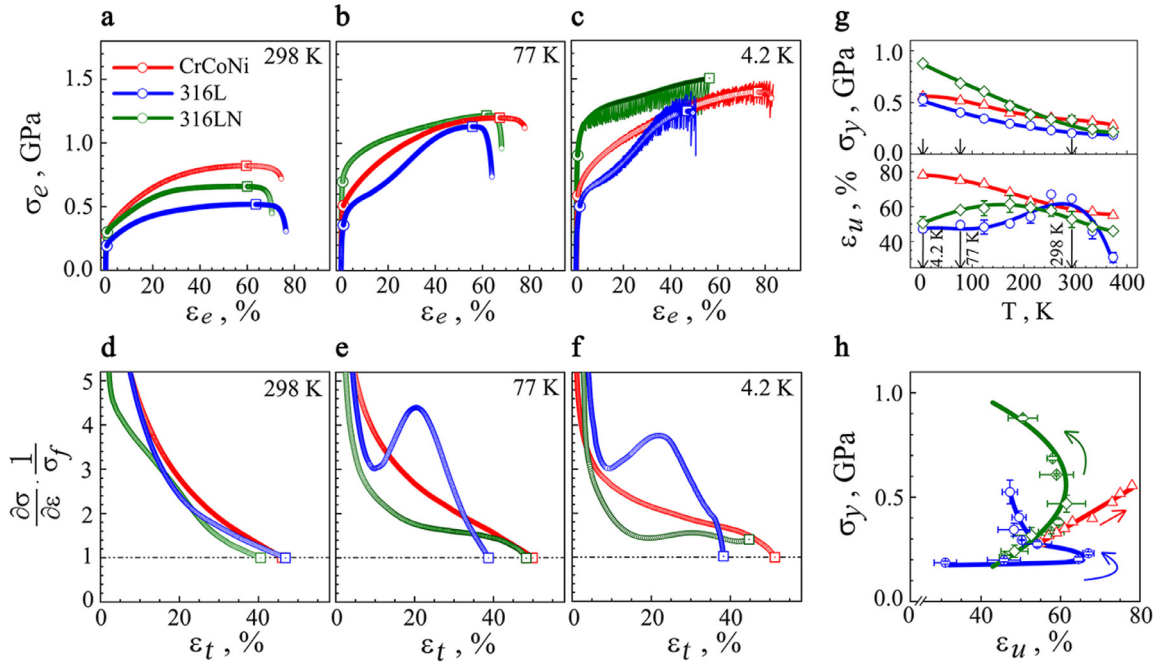

Fig. 2. Tensile properties of CrCoNi, 316L, and 316LN. (a–c) Tensile engineering stress-strain curves ($\sigma_e - \varepsilon_e$) in CrCoNi, 316L, and 316LN, respectively, at 298 K (a), 77 K (b), and 4.2 K (c). Red line: CrCoNi, blue line: 316L, green line: 316LN. Circle: yield strength, Square: ultimate tensile strength (UTS). Note the presence of serrated flow at 4.2 K (c). (d–f) Strain hardening rate ($^{\partial\sigma}/_{\partial\varepsilon}$) normalized by flow stress (σ_f) vs true strain (ε_t) curves at three temperatures in the three alloys. Square: uniform elongation. (g) Yield strength (σ_y) (upper panel) and uniform elongation (ε_u) (lower panel) vs testing temperatures ranging from 373 K to 4.2 K in CrCoNi, 316L, and 316LN, respectively. Note the rise at first and drop later in ε_u in both 316L and 316LN, in sharp contrast to the monotonic rise in CrCoNi. (h) (σ_y, ε_u) balance in the three alloys. Arrows show the trend with decreasing temperature.

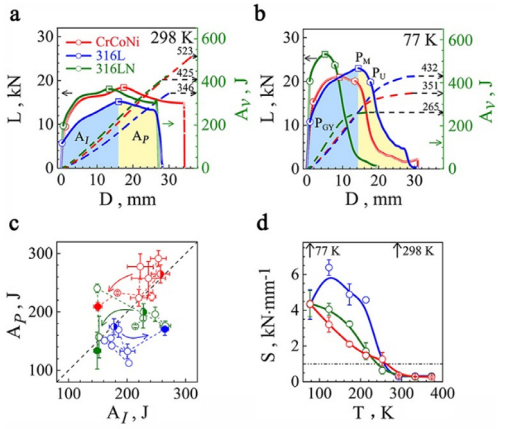

Fig. 3. Full-size Charpy V-notch impact properties in CrCoNi, 316L, and 316LN. (a) and (b) Load–deflection (L–D) curves (left y-axis, solid lines) and absorbed energy–deflection (A_v–D) curves (dashed lines by integrating the L–D curves, right y-axis) at 298 K and 77 K, respectively. P_{GY} and P_M are yield load and peak load, respectively. P_U indicates the onset of unstable fracture propagation. A_K: Charpy impact energy (number as indicated by arrows towards right y-axis). A_I: crack initiation absorbed energy (blue area under L–D curve before P_M). A_P: crack propagation absorbed energy (yellow area under L–D curve after P_M). (c) Balance of A_I and A_P in the three alloys with temperatures ranging from 373 K to 4.2 K. Solid and half-open symbols represent A_I and A_P at 77 K and 298 K. (d) Change of slope with applied temperatures after P_U in the three alloys.

3.2.2. Full-size Charpy V-notch impact toughness (A_K)

Fig. 3(a) and (b) summarizes the load–deflection (L–D) curves and absorbed energy–deflection curves at 298 K and 77 K, respectively, in CrCoNi, 316L, and 316LN. The L-D curves at other temperatures are displayed in Fig. S2. Optical micrographs of all Charpy V-notch (CVN) specimens after impact loading are displayed in Fig. S3.

Usually, the total impact absorbed energy (A_K) consists of two parts, i.e., the crack initiation absorbed energy (A_I) and the crack propagation absorbed energy (A_P), as schematically marked in Fig. 3(b). A_K was 523, 346, and 425 J at 298 K and 351, 432 and 265 J at 77 K in the three alloys. Obviously, A_K of CrCoNi is the largest, and that of 316L is the smallest at 298 K. Moreover, when going to 77 K, both yield load (P_{GY}) and maximum load (P_M) are dramatically increased in 316LN, see Fig. 3(b), overtaking those in CrCoNi. However, crack initiation and crack propagation in 316LN occur earlier, resulting in a lower A_K value of 265 J at 77 K. The A_K of CrCoNi slightly decreases when compared to 298 K, but the value remains very high at 351 J. Surprisingly, 316L has a higher A_K of 432 J at 77 K, compared with 346 J at 298 K. This observation differs from those previously reported in austenitic stainless steels [40–44], where A_K was found to be gradually reduced with decreasing testing temperature. The increase of A_K in 316L is related to the crack initiation absorbed energy (A_I). As shown in Fig. 3(c), A_I of 316L shows significant increase and A_P has not changed much at 77 K, compared with those at 298 K. A_I and A_P obviously decrease in CrCoNi and 316LN, when the temperature is reduced to 77 K. The rate of unstable crack expansion can be obtained by fitting the L–D curves after P_U, see Fig. 3(d). The slopes increase about one order of magnitude with decreasing temperature to 77 K in the three alloys. 316L has a slightly higher rate at lower temperatures than CrCoNi and 316LN.

3.2.3. Fracture toughness (K_C)

To compare with toughness data published for CrCoNi [18], the nonlinear-elastic fracture mechanics analysis was used to determine the J-based crack-resistance curves (the J-integral vs crack extension Δa curves, i.e., R curves) of stainless steels, calculated from the force vs load-line displacement data, as displayed in Fig. 4. The J-integral value of crack initiation was determined by the intersection point of J–Δa curves and the 0.2 mm offset blunting line [33],

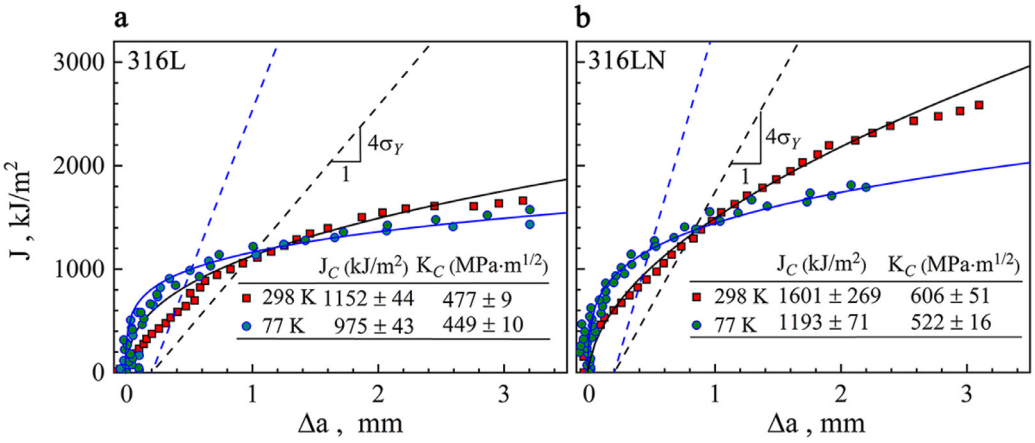

Fig. 4. Fracture toughness through compact-tension C(T) specimen testing in 316L and 316LN. An increasing fracture resistance in terms of the *J*-integral vs crack extension Δa (i.e., resistance curve, R curve) in 316L (a) and 316LN (b) at 298 K and 77 K, respectively. According to ASTM standard [33], a power law, $J = C_1(\Delta a)^{C_2}$, is adopted to fit the data, see solid lines. Dashed lines are construction lines ($J = M\sigma_Y \Delta a$, $M = 4$ for high work-hardening materials, effective yield strength $\sigma_Y = (\sigma_y + UTS)/2$) with 0.2 mm offset. See inserted tables for the values of J_C and K_C at 298 K and 77 K, respectively.

$$J = M\sigma_Y \Delta a. \quad (1)$$

where $M = 4$, suitable for high work-hardening materials, such as austenitic stainless steels [29,33], σ_Y is the effective yield strength, $\sigma_Y = (\sigma_y + UTS)/2$, UTS is the ultimate tensile strength.

In our tests, J_C cannot be taken as J_{IC}, because J–Δa curve obtained in Fig. 4 does not meet the ASTM standard to measure fracture toughness under plane strain [33], see Eq. (2), due to inadequate sample thickness and very high J_C of stainless steels in the present investigation.

$$B, b_0 > \frac{10J_C}{\sigma_Y}, J < b_0\sigma_Y/7.5 \quad (2)$$

where B is the sample thickness and b_0 the initial ligament size.

The J_C value is 1152 kJ/m^2 at 298 K and 975 kJ/m^2 at 77 K for 316L, see Fig. 4. For 316LN, the J_C value is as high as 1601 kJ/m^2 at 298 K and 1193 kJ/m^2 at 77 K. For CrCoNi [18], the J_C (K_{JIC}) value is 212 kJ/m^2 (208 MPa m$^{1/2}$) at 293 K and 363 kJ/m^2 (273 MPa m$^{1/2}$) at 77 K. In order to compare fracture toughness of both 316L and 316LN with CrCoNi, K_C is obtained from *J*-integral value of crack initiation (J_C), using $K_J = \sqrt{(E'J_{IC})}$, where $E' = E/(1-\nu^2)$. The K_C value of 316L is 477 MPa m$^{1/2}$ at 298 K and decreases to 449 MPa m$^{1/2}$ at 77 K, see Fig. 4(a), and that of 316LN, see Fig. 4(b), is 606 MPa m$^{1/2}$ and 522 MPa m$^{1/2}$ at 298 K and 77 K, respectively. Therefore, K_C drops with T in both 316L and 316LN, with a rising trend of K_C in CrCoNi [18]. Moreover, K_C of 316LN is a bit higher than that of 316L, and both the 316L and 316LN show higher fracture toughness than that in CrCoNi across the whole temperature range.

3.2.4. Micro-hardness distribution around crack tip after impact and toughness tests

The Vickers micro-hardness (HV) measurement was performed near the crack tip and along the cracking path, to quantify the strain hardening behavior after the impact and fracture toughness testing in 316L and 316LN, see Fig. 5. Similar results for CrCoNi can be found in Refs. [21,22]. Clearly, an enhanced HV appears within a large area at the tip of crack propagation in CVN and C(T) samples, see Fig. 5(a) and (b). For C(T) specimens of 316L and 316LN, the area showing strain hardening to varying contents, with an enhancement of HV, is almost similar to the shape of the plastic zone in a plane strain state [45], although the plane strain condition is not completely satisfied in the present testing. Fig. 5(c) shows the maximum increment of HV (ΔHV) and the size of hardening zone (r_c). The ΔHV values for the 316L CVN sample are 2.4 and 2.8 GPa at 298 K and 77 K, respectively, and the corresponding r_c is 9.6 and 6.6 mm. By comparison, ΔHV for C(T) samples is 2.3 and 2.7 GPa at 298 and 77 K, respectively, and r_c is 7.9 and 6.0 mm. For 316LN, ΔHV for CVN sample is 2.7 and 3.2 GPa at 298 K and 77 K and r_c is 7.8 and 5.6 mm, ΔHV for C(T) samples is 2.4 and 3.0 GPa and r_c is 6.2 and 5.0 mm at 298 K and 77 K. Obviously, ΔHV increases with the drop of T from 298 K to 77 K for both the impact and fracture toughness testing in these two alloys, while r_c decreases quickly. This indicates the strong dependence of work-hardening with T, which is closely associated with the microstructural evolution at cryogenic temperatures. Also, 316L has a larger r_c but a smaller ΔHV, compared with 316LN, for both CVN and C(T) samples at the same testing temperature.

3.3. Microstructures after mechanical loading

3.3.1. XRD analysis after tensile and Charpy impact tests

Fig. 6 collects the XRD spectra before and after tensile and impact testing at 298 K, 77 K, and 4.2 K, respectively, for CrCoNi, 316L, and 316LN. All three alloys are of a single-phase FCC structure before testing, consistent with the EBSD analysis (Fig. 1). The volume fraction of FCC (V_{FCC}) before and after deformation is summarized in Table 2. In Fig. 6(a), only FCC peaks can be seen after tensile and impact testing in CrCoNi, indicating that FCC is stable against phase transition even after high-rate impact deformation at 4.2 K. Fig. 6(b) and (c) displays a single FCC phase in 316L and 316LN after tensile testing at 298 K. In contrast, V_{FCC} in 316L decreases to 24% and 20% after tensile testing and 68% and 70% after impact testing, at 77 K and 4.2 K. V_{FCC} in 316LN reduces to 62% and 57% after tensile testing at 77 K and 4.2 K, respectively. Upon impact testing at two lower temperatures in 316LN, however, phase transformation hardly happens, due to the improvement of austenite stability with the addition of nitrogen in stainless steels [34,46,47]. Therefore, it turns out that austenite in CrCoNi is the most stable against mechanical deformation among the three FCC alloys.

3.3.2. Microstructural evolution during tensile testing

Both the EBSD and TEM observations were then conducted to investigate the microstructural evolution, along with phase transformation after various straining in both 316L and 316LN.

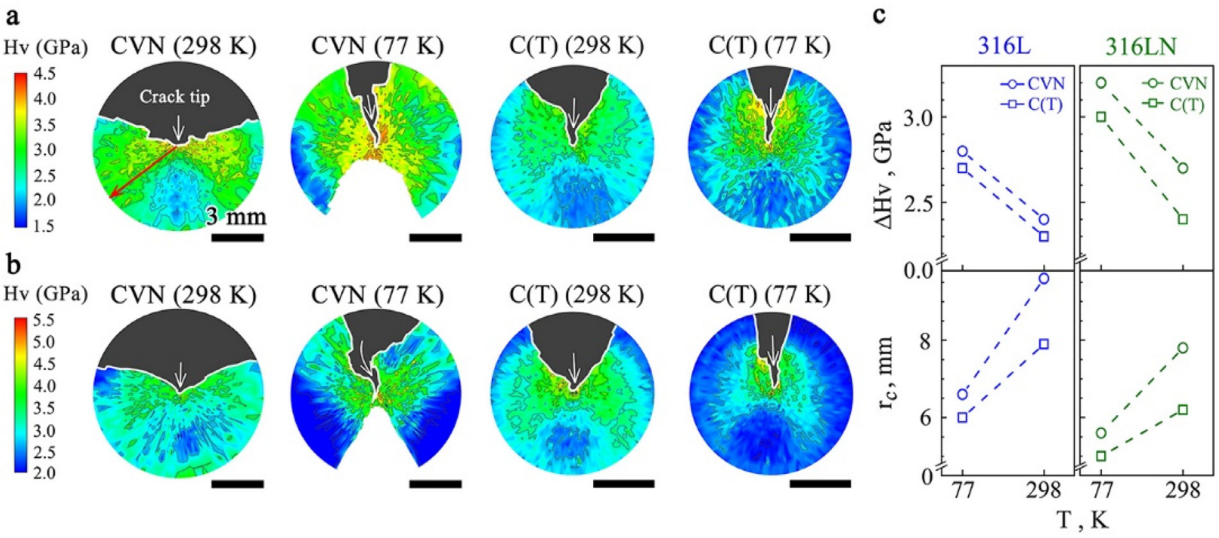

Fig. 5. HV distribution of Charpy V-notch impact (CVN) and compact-tension (C(T)) specimens at 298 K and 77 K. (a) and (b) HV profiles ahead of the crack tip and along the cracking path in 316L and 316LN, respectively. White arrow: crack tip. White line: crack propagation path. HV distribution along the red arrow is plotted in Fig. S4, showing the gradient change of HV across the plastic zone. (c) ΔHV (HV increment at crack tip) and r_c (the hardening zone size) for CVN and C(T) specimens at 298 K and 77 K in 316L (left column) and 316LN (right column), respectively. All scale bars are the same of 3 mm.

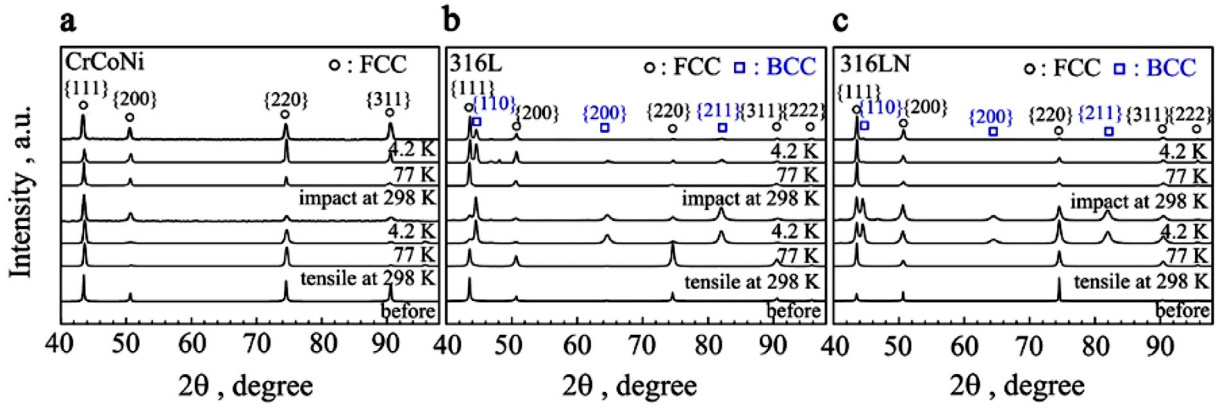

Fig. 6. XRD spectra before and after tensile and impact testing at 298 K, 77 K, and 4.2 K, respectively: (a) CrCoNi, (b) 316L, (c) 316LN.

Table 2
Volume fraction of FCC (V_{FCC}, %) before and after tensile test, impact toughness test, and fracture toughness test in CrCoNi, 316L, and 316LN, estimated from XRD and EBSD analysis. The testing temperatures (298, 77, and 4.2 K) are given in the second row. Black and blue numbers: V_{FCC} estimated from XRD and EBSD, respectively.

Material	Before	After tensile test			After impact toughness test			After fracture toughness test		
		298	77	4.2	298	77	4.2	298	77	4.2
CrCoNi	100	100	100	100	100	100	100	100	100	100
316L	100	100/99	24/8	20/6	100/99	68/67	70/60	99	57	–
316LN	100	100/99	62/30	57/37	100/99	99/99	99	100	86	–

Fig. 7(a–c) and Fig. 7(d–f) are EBSD images of 316L and 316LN after tensile testing, respectively. For 316L at 298 K (Fig. 7(a)), the generation of slip bands, along with deformation twins (inset), is typical of the microstructural features to respond to tensile straining. Usually, two systems of both the slip-bands and deformation twins (DTs) are activated. Fig. 7(g) is the TEM image showing the DTs. The dislocations and DTs, along with their interactions, induce strain hardening in 316L. With the drop of T to 77 K, the bcc-structured martensite (α') is produced, see Fig. 7(b) and the inset phase image. Fig. 7(h) is the TEM image, further showing the presence of α', by indexing in the $[\bar{1}11]$ zone axis (z.a.). With T further decreasing to 4.2 K, see Fig. 7(c), the main plastic accommodation is still the martensitic transformation. The difference lies in the presence of ε-phase apart from α', see Fig. 7(i). The two insets are SAED patterns of the $\alpha'$and ε-phase, respectively.

The microstructural response in 316LN is similar to that in 316L. At 298 K, profuse DTs carry the main plastic deformation, see Fig. 7(d). When decreasing T down to 77 K (Fig. 7(e)) and 4.2 K (Fig. 7(f)), respectively, martensitic transformation happens. However, martensite phase transformation in 316LN is not as much as that in 316L, when comparing the values of V_{FCC} shown in Table 2.

3.3.3. Microstructural response upon impact loading

Fig. 8 reveals the microstructural response during impact deformation in 316L. The main crack (C1) appears passivated at 298

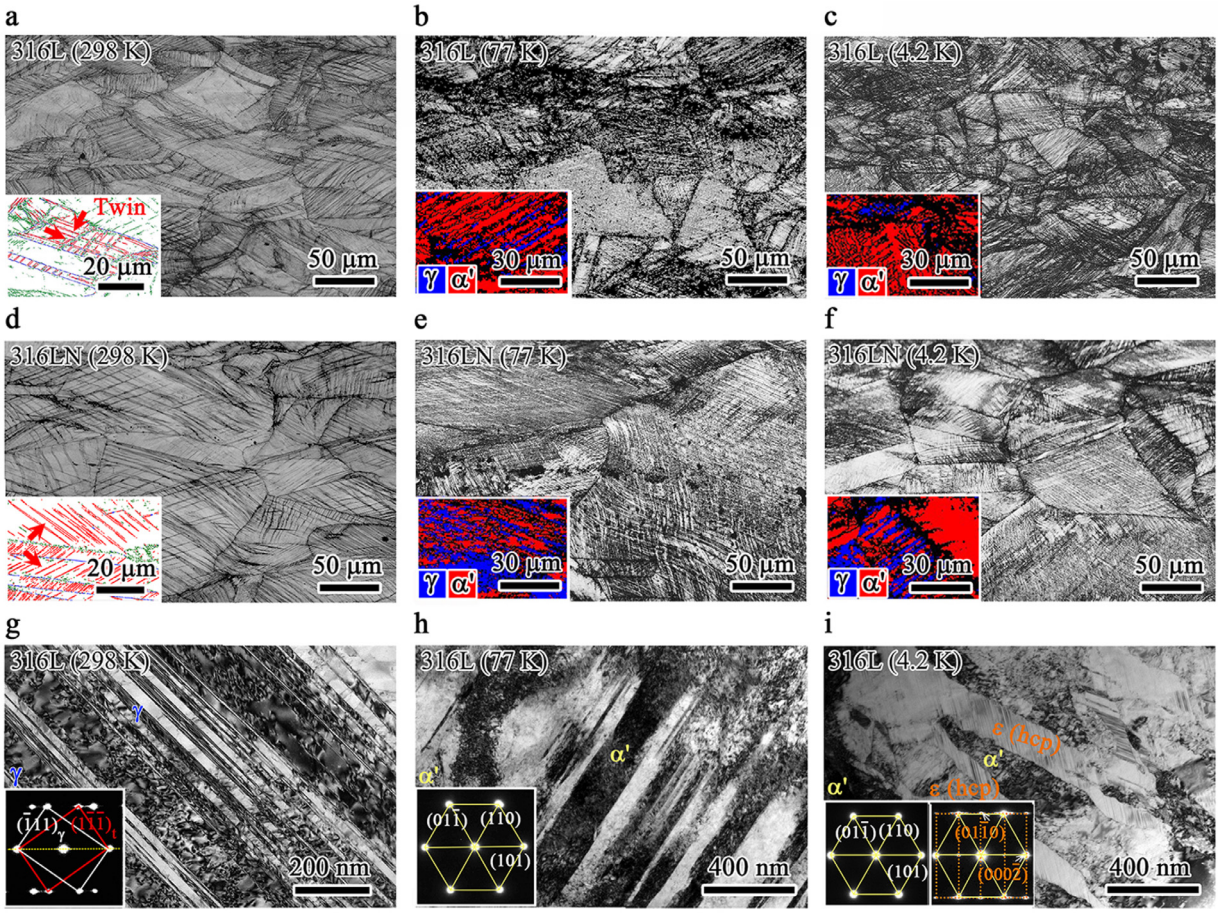

Fig. 7. Microstructure after tensile deformation at varying temperatures in 316L and 316LN. (a–c) and (d–f) EBSD images in 316L and 316LN, respectively, at 298 K, 77 K, and 4.2 K. Inserts in (a) and (d): grain boundary (GB) map. Red: Σ3 twin boundary. Green: LAGB. Blue: HAGB. Arrows: twins. Insets in (b), (c), (e) and (f): phase map. Red area: martensite (α'). Blue area: austenite (γ). (g–i) Bright-field TEM images in 316L at 298 K, 77 K, and 4.2 K, respectively. (g) Twin plates in γ. Inset: the selected area electron diffraction (SAED) pattern with the [110] zone axis (z.a.). (h) α' in γ. Inset: the SAED pattern of α' with the $[\bar{1}11]$ z.a. (i) The evidence of both α' and ε in γ. Insets: the SAED patterns of α' and ε, respectively, with the $[\bar{1}11]$ z.a. and $[2\bar{1}\bar{1}0]$ z.a.

K, see Fig. 8(a) (upper panel). There are two secondary cracks (C2) along the crack propagation path. Close-up view near C2, see Fig. 8(b) (upper panel), shows the formation of shear bands (SBs) emitted from the crack tip, together with DTs of high density. The single-phase FCC is kept during impact loading, see phase images in Fig. 8(a) and (b) (lower panel). Fig. 8(c) is the close-up view of the dashed box in Fig. 8(b). The spreading SBs of two orientations are clearly seen, along with TBs. When T drops to 77 K in 316L, there is a huge difference in the microstructural response from that at 298 K, see Fig. 8(d) and (e), near the main crack and secondary crack, respectively. It is interesting to observe the α'-bands near the crack tip, see red strips in phase images. The SBs are, actually, the precursor of these α'-bands. It is strain localization inside these SBs that induces phase transformation. α' causes strain hardening, which is the reason for an increase in A_l at 77 K as compared to that at 298 K (Fig. 3(a) and (b)). Fig. 8(f) shows a void inside one plate, and α' of high density is visible at the void edge.

The microstructural evolution in 316LN upon impact loading is shown in Fig. 9. At 298 K, SBs, slip bands, and DTs are all visible near the tip of either the main crack (Fig. 9(a)) or secondary crack (Fig. 9(b)). α' is hardly detectable, as evidenced in the EBSD phase image (lower panel) of Fig. 9(a) and inset of Fig. 9(b). It turns out that there is no phase transformation during impact testing at 298 K. At 77 K, similar microstructural responses are observed to those at 298 K, including the SBs, slip-bands, and DTs of high density. However, a small amount of α' is observed in SBs, see inset in Fig. 9(c) and almost no α' exists inside SBs at the tip of secondary crack (Fig. 9(d)).

3.3.4. Microstructural response during fracture loading

For 316L, the path of crack propagation of low magnification is shown in Fig. 10(a) in a C(T) sample subjected to fracture toughness testing. The close-up views, see Fig. 10(b) and (c), show the presence of SBs and slips at 298 K, together with DTs of high density. SBs usually emit from the crack tip. Martensitic transformation is negligible, see phase map (lower panel) in Fig. 10(b). When it comes to 77 K, phase transformation dominates particularly along the propagating path of crack, see lower panels in Fig. 10(e) and (f). Phase transformation happens not only inside the individual grain but also inside the SBs. V_{FCC} is measured to be 57% based on the EBSD analysis, a little lower than that after impact loading at 77 K (Table 2).

For 316LN, both the path of crack propagation (Fig. 11(a)) and microstructural evolution (Fig. 11(b) and (c)) at 298 K are similar to those in 316L. No phase transformation occurs. The presence of high density of LAGB indicates profuse dislocation activities in the plastic zone ahead of the crack tip. Deformation twinning is also observed, but not as profuse as dislocation activities, as shown in Fig. 11(c). When the temperature decreases to 77 K (Fig. 11(d)), phase transformation takes off in Fig. 11(e) and (f). The V_{BCC} value around crack tip after fracture at 77 K is 14% measured

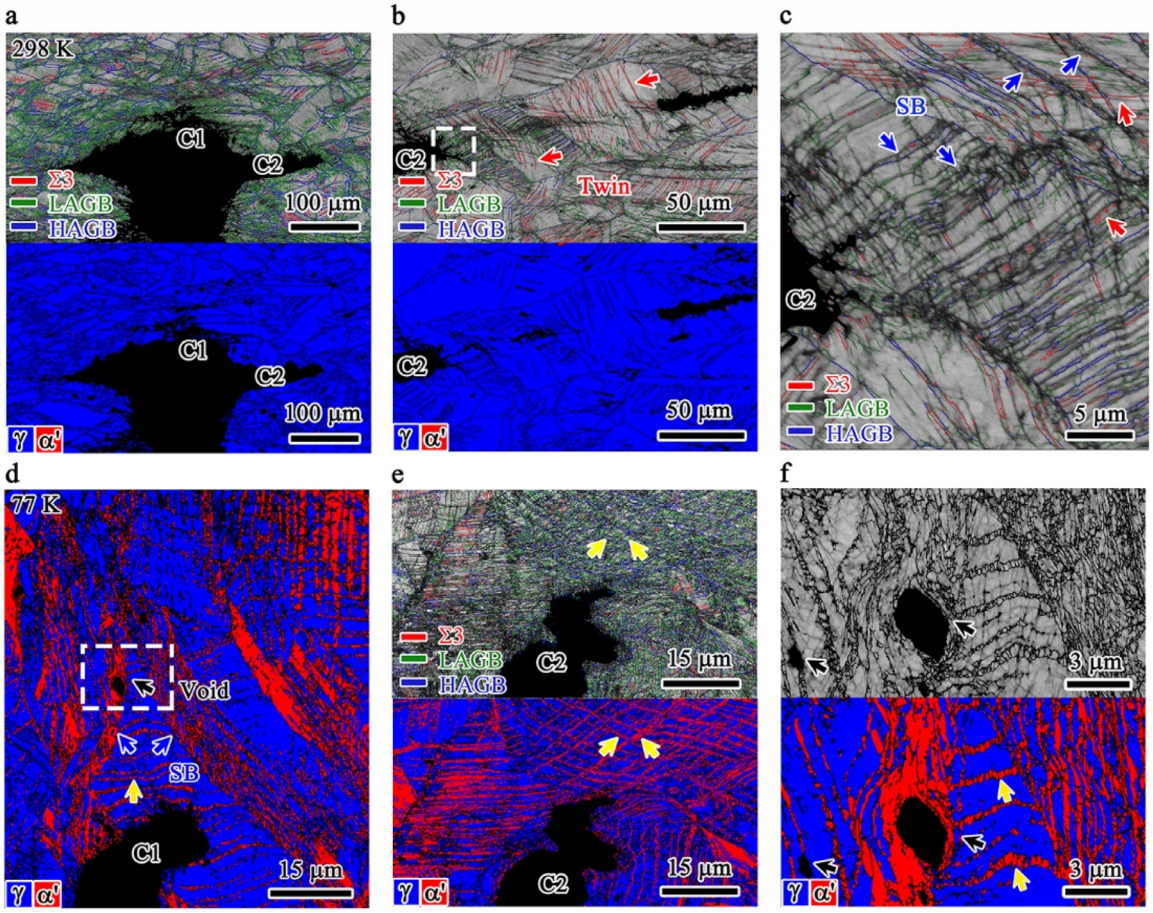

Fig. 8. Microstructural evolution near crack tip after impact testing at 298 K and 77 K in 316L. (a) EBSD image quality (IQ) map showing the boundary features at the tip of the main crack (C1) at 298 K (upper panel). Red: Σ3 twin boundary. Green: LAGB. Blue: HAGB. Note that there is no phase transformation, see phase image (lower panel). (b) EBSD image at the tip of secondary crack (C2) (upper panel). Note the presence of deformation twins of high density. Lower panel: phase image. Red arrow: twin boundaries. (c) Close-up view of the dashed area in (b). Blue arrows: shear bands of two orientations. (d) Phase map at the tip of the main crack (C1) at 77 K. Note the production of a large amount of α' (red area) in SBs. Also, note the formation of micro-voids, one is shown by the arrow. (e) IQ image with GB (upper panel) and phase image (lower panel) at the tip of secondary crack (C2). (f) Close-up view of the dashed box in (d), showing the formation of micro-void inside the first SB (black arrows), along with the production of plenty of second SBs (yellow arrows). Note α' in secondary SBs *via* phase transformation upon impacting especially at cryogenic temperatures.

from the EBSD phase map (Fig. 11(e)). In a nutshell, in the fracture toughness testing of 316LN, the mechanism of plastic deformation changes from the dislocation slip and twinning at 298 K to dislocation slip, twining and martensitic transformation at 77 K.

3.4. Fracture surface morphology

Fig. 12 illustrates the fractography of CVN samples in 316L and 316LN by SEM. For 316L, only initiation (I) and stable crack propagation (P) areas are visible at 298 K (Fig. 12(a)). The close-up view in P, see Fig. 12(b), shows elongated coarse dimples, due to the ductile austenite. When it comes to 77 K, largely unstable crack propagation (U) and shear-lip (S) areas are also visible (Fig. 12(c)). Dimples are heterogeneous, see enlarged view in P (Fig. 12(d)). To be specific, dimples of the two sizes are easily discernable at 5 μm and 15 μm, respectively. For 316LN, similar fractography is displayed at 298 K (Fig. 12(e)), and the dimples are uniform (Fig. 12(f)). At 77 K, unstable crack propagation occurs in Fig. 12(g). As shown in Fig. 12(h), some dimples and cleavages are produced at the fracture surface.

The fractography of C(T) samples after fracture toughness loading in 316L and 316LN is displayed in Fig. 13. It shows pronounced stretch-zone at crack initiation in 316 L at 298 K, consistent with the obvious passivation at crack tip (Fig. 10(a)). In Fig. 13(b), there are numerous equiaxed coarse dimples in the fracture zone. At 77 K, the size of the stretch-zone is reduced as shown in Fig. 13(c). Dimples are heterogeneous (Fig. 13(d)). It has been recognized that the fine dimples arise from martensite and large dimples correspond to the fracture of austenite [44]. For 316LN, a more pronounced stretch-zone occurs at crack initiation (Fig. 13(e)), compared with 316L at 298 K. Typical large and deep coarse dimples with a diameter larger than 100 μm are observed on the fracture surface (Fig. 13(f)). When it comes to 77 K, the size of the stretch-zone decreases (Fig. 13(g)) and plenty of little dimples appear (Fig. 13(h)).

4. Discussion

4.1. Strength-toughness balance in three alloys

Fig. 14 summaries the strength-toughness balance in CrCoNi, 316L, and 316LN, together with data in other alloys for comparison [12,18,21,22,29,43,44,48–65]. Fig. 14(a-1) and (a-2) show A_K and K_C vs T curves, respectively. CrCoNi excels with excellent A_K at various T (Fig. 14(a-1)) and the best combination of A_K and UTS (Fig. 14(b-1)). A_K of 316LN is greater than that of 316L above 123 K, while 316L performs better below 123 K, due to the increase of A_K in 316L when decreasing T further below 200 K. K_C of both 316L and

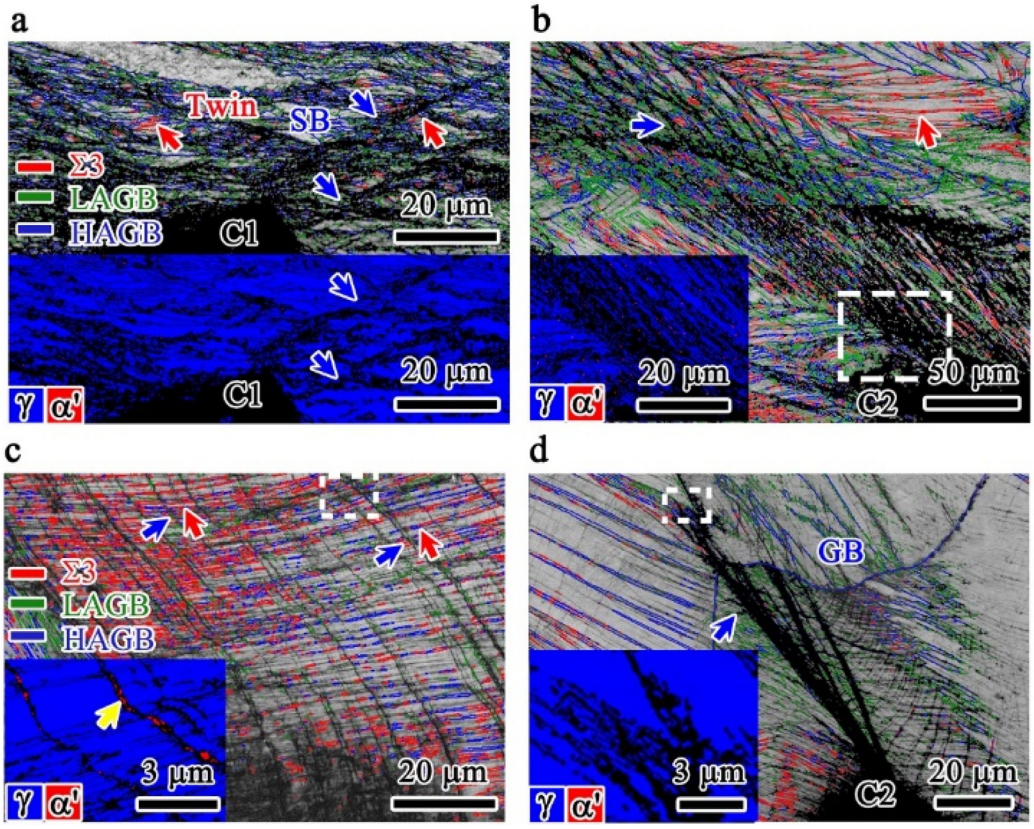

Fig. 9. Microstructural evolution near the crack tip after impact testing at 298 K and 77 K in 316LN. (a) EBSD IQ (upper panel) and phase image (lower panel) map at the tip of main crack (C1) at 298 K. Note the prevalent shear bands (blue arrows), along with deformation twins (red arrows). Also, note there is no phase transformation inside SBs (arrows in lower panel). (b) EBSD IQ image overlapping with GB image (upper panel), along with phase image (insert) at the tip of secondary crack (C2). Note the high density of slender SBs and twins. (c) EBSD IQ image overlapping with GB image near the path of crack propagation at 77 K. Note the presence of SBs and twins of high density. (d) IQ image at the tip of secondary crack (C2). Note only few α' inside SBs as shown in phase maps of two insets.

Table 3
Deformation mechanisms operating during tensile test, impact toughness test, and fracture toughness test in CrCoNi, 316L, and 316LN. The testing temperatures (298, 77, and 4.2 K) are given in the second row.

Material	Deformation mechanism after tensile test		Deformation mechanism after impact toughness test		Deformation mechanism after fracture toughness test	
	298	77	298	77	298	77
CrCoNi	Lots of twins, dislocations [16,24]	Twins of higher density, dislocations [16,24]	Profuse twins ahead of and inside the SBs [22]	Finer twins ahead of and inside the SBs [21,22]	Lots of twins, dislocations [18]	Twins of higher density, dislocations [18]
316L	Lots of twins, dislocations	Massive martensitic transformation	Profuse twins and dislocations ahead of SBs	Martensite formation inside the SBs	Lots of twins, dislocations	Martensite formation inside the SBs and grains
316LN	Lots of twins, dislocations	Martensitic transformation, dislocations	Profuse twins and dislocations ahead of SBs	Twins ahead of SBs and few martensite inside the SBs	Lots of twins, profuse dislocations	Lots of twins, dislocations, few martensite

316LN is much higher than that of CrCoNi [18] and other alloys [12,29,58–64], along with an excellent strength-toughness combination (Fig. 14(b-2)). Meanwhile, K_C of 316LN is slightly better than that of 316L. Furthermore, K_C of 316L and 316LN decreases with the decrease of T, while that of CrCoNi increases.

The deformation mechanisms, including deformation twinning, dislocation motion, as well as phase transformation, change with strain rate and testing temperature. They greatly influence the macroscopic mechanical properties, in particular strain hardening, which will be discussed next. The main deformation mechanisms of these three alloys are also summarized in Table 3.

4.2. Influence of temperature on strain hardening mechanism

4.2.1. Hardening mechanism transition with decreasing temperature upon tensile testing

Fig. 2 shows similar strength and plasticity for all three alloys at 298 K, and the strain hardening rate decreases monotonously with strain. As shown in Fig. 7(a) and (d), the generation of slip bands, along with the activation of DTs provide the main hardening mechanisms in 316L and 316LN at 298 K. In CrCoNi, planar dislocation slip, the interactions of dislocations and three-dimensional deformation twin network dominate the deformation [16,17,24].

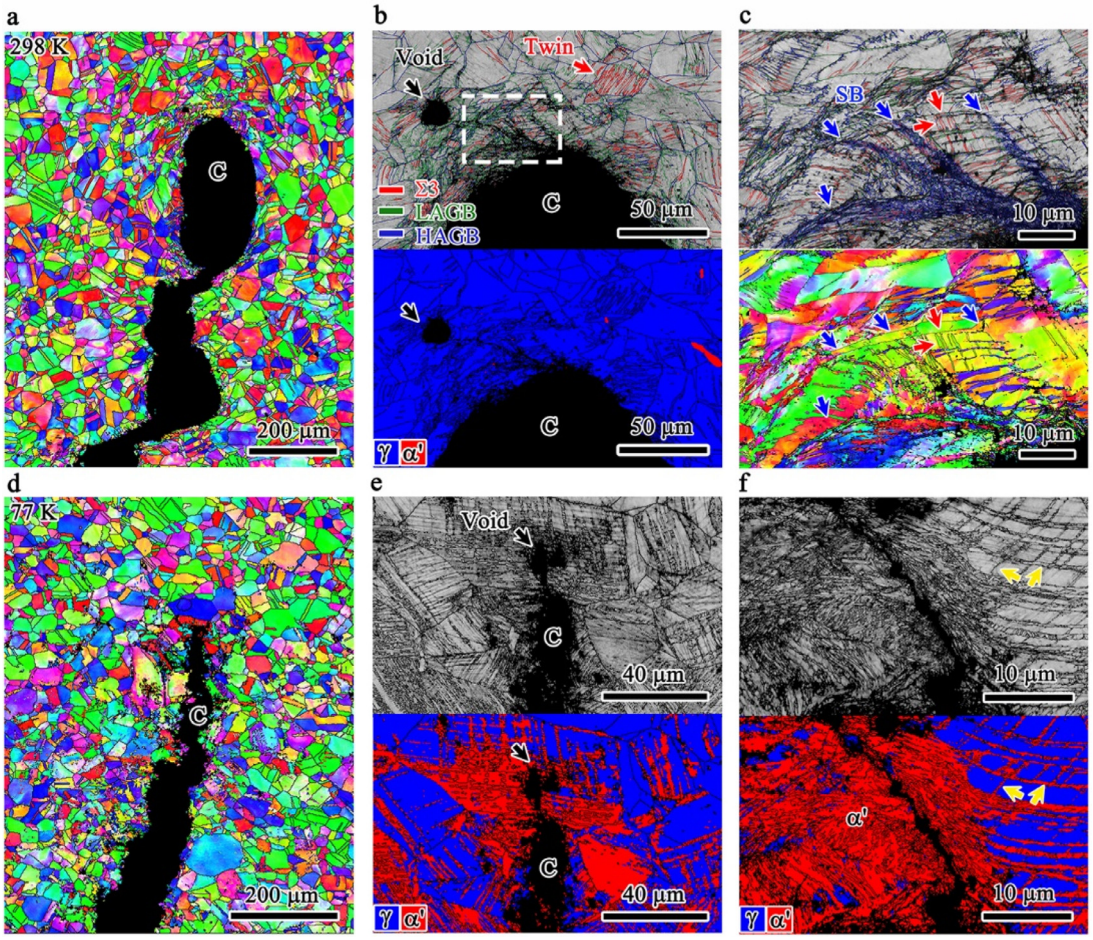

Fig. 10. Microstructural evolution near the crack tip after fracture toughness testing at 298 K and 77 K in 316L. (a) EBSD IPF image showing the propagating path of crack (C) at 298 K. (b) Close-up view of the crack tip. Note the production of SBs and twins (red arrows) of high density, along with micro-voids (black arrow), as shown in IQ image (upper panel). Only a few α' is observed, see phase map (lower panel). (c) Close-up view of the white box in (b), clearly showing the SBs (blue arrows) and twins. (d) IPF map along the propagation path of crack (C) at 77 K. (e) Close-up IQ and phase map of the crack tip. The α' formation *via* phase transformation is evident, see phase image (lower panel), inside both SBs and grains. (f) α' formation along cracking path inside both SBs (yellow arrows) and grains.

With the drop of temperature, a two-stage strain hardening behavior occured in 316L and 316LN at 77 K and 4.2 K. While a clear up-turn of strain hardening rate occurs in 316L, a relatively weak two-stage hardening behavior is seen in 316LN. Previous studies have shown that the up-turn is related to the austenite-martensite transformation, and α'-martensite forms at the onset of the second stage [38,39]. As shown in Fig. 7(b) and (c), mechanically-driven martensitic transformation occurs in 316L, and only 24% of V_{FCC} remains after tensile at 77 K and 20% at 4.2 K (Table 2). The martensitic transformation causes the re-acceleration of strain hardening in 316L. In 316LN, on the other hand, V_{FCC} remains 62% and 57% after tensile at 77 K and 4.2 K, respectively, due to the improvement of austenite stability with the addition of nitrogen. As a result, the martensitic transformation in 316LN is not as much as that in 316L and cannot provide sufficient hardening as that in 316L. Therefore, a much slower drop and a weak up-turn of strain-hardening occurs under higher strain in 316LN at 77 K and 4.2 K, respectively. In CrCoNi, deformation twinning occurs earlier due to its low SFE and the increase of stress level with decreasing temperature. The twins of higher density provide continuous hardening, along with better strength-ductility combination [16,24].

4.2.2. Hardening mechanism transition with decreasing temperature upon impact testing

Both the 316L and 316LN exhibit, actually, the transition of plastic deformation mechanism during impact as the temperature drops. The dislocation activities and DTs reign at 298 K in 316L (Fig. 8(b) and (c)). Strong strain hardening is thus provided. SBs are generated as a result of strain localization at the tip of the notch. DTs form continuously and dynamically along with deformation to effectively delay the propagation of SBs. That is to say, DTs and associated strain hardening are advantageous for extending the plastic deformation zone and promoting fracture resistance. At 77 K, transformation-induced plasticity (TRIP) comes in. The mechanically-driven α' forms in large quantity in SBs in 316L (Fig. 8(e) and (f)). This TRIP effect provides work-hardening to stabilize SBs. This is self-toughening, leading to de-localization in SBs, which alleviates softening of SBs, similar to the effect of nanoscale twins inside SBs in CrCoNi [21,22]. Therefore, as shown in Fig. 5, a large plastic zone (r_c is 6.6 mm for 316L, larger than the ~5.6 mm for 316LN) forms, which is a distinctly different mechanism from deformation twinning induced hardening at 298 K. Hence, an increase in A_I (in Fig. 3(c)) and A_K are obtained in 316L at 77 K.

In 316 LN, dislocation slips and DTs are the dominant mechanism of plastic deformation at 298 K (Fig. 9(a) and (b)), as well as that in 316L. At 77 K, both DTs and α' occur in 316LN (Fig. 9(c)). The DTs are triggered by SBs and their interactions with DTs delay the expansion of advancing SBs. Meanwhile, some martensitic transformation assists the deformation inside SBs (inset of Fig. 9(c)). In contrast, martensitic transformation hardly happens in 316LN, compared with 316L at 77 K. It is known that nitrogen

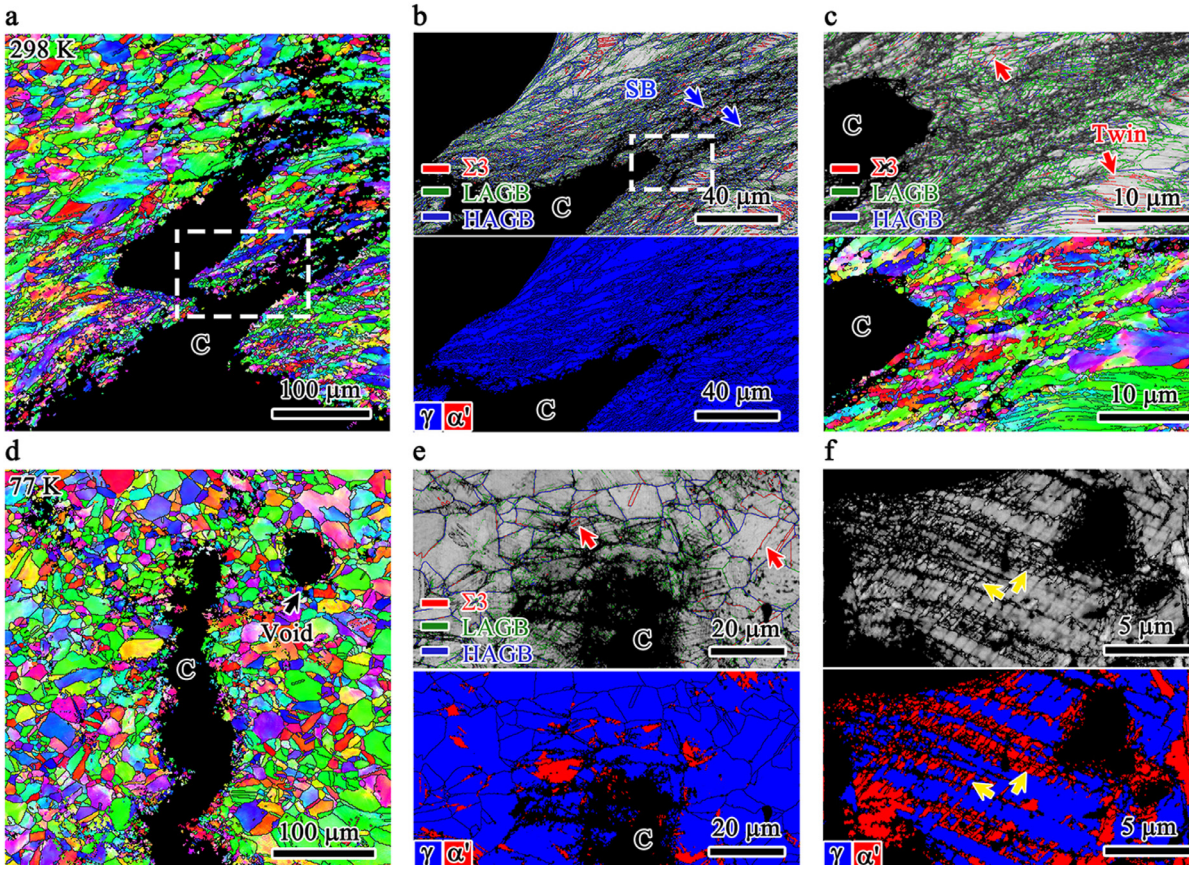

Fig. 11. Microstructural evolution near the crack tip after fracture toughness testing at 298 K and 77 K in 316LN. (a) EBSD IPF image showing the propagating path of crack (C) at 298 K. (b) Close-up view of the dashed box in (a). Note the SBs of high density (upper panel). No α' is observed, see phase image in the lower panel. (c) Close-up view of the white box in (b), clearly showing the LAGBs of high density, along with twins. (d) IPF map along the propagation path of crack (C) at 77 K. See a large void nearby (black arrow). (e) Close-up IQ map (upper panel) and phase map (lower panel) of the crack tip. (f) Close-up view along crack paths. The α' formation *via* phase transformation is evident, see phase image inside both SBs (yellow arrows) and grains.

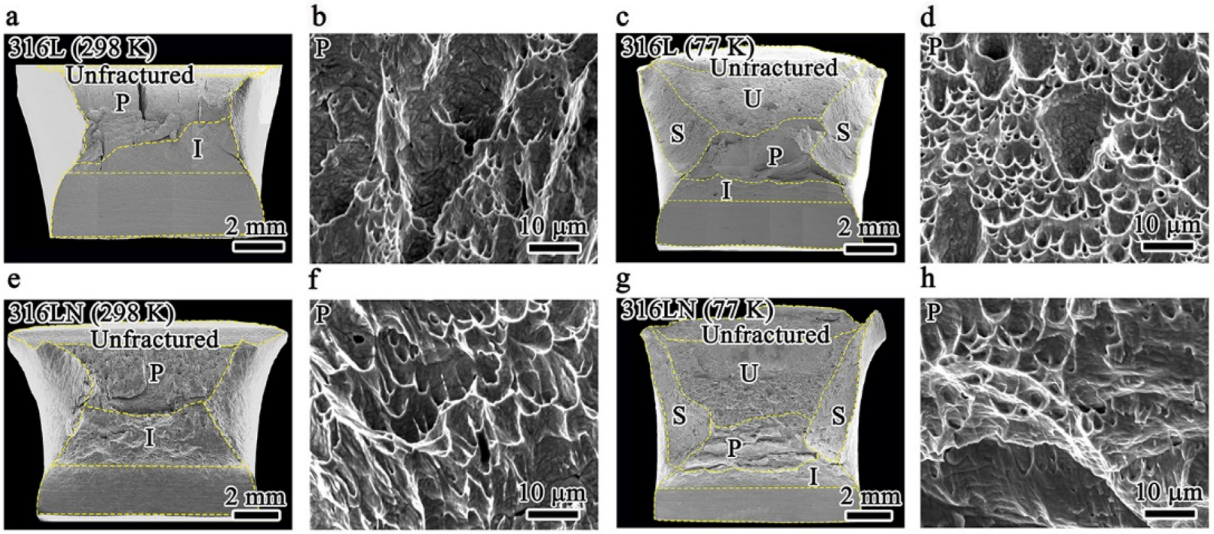

Fig. 12. Fractography after impact testing in 316L and 316LN. (a) Fracture surface of 316L at 298 K. Only initiation (I) and stable crack propagation (P) area are visible. (b) Close-up image in P area. (c) Fracture surface of 316L at 77 K. Besides I and P, large unstable crack propagation (U) and shear-lip (S) areas are also visible at 77 K. (d) Close-up image in P area. (e) and (f) Fracture surface and close-up image in P area in 316LN at 298 K, respectively. (g) and (h) Fracture surface and close-up image in P area in 316LN at 77 K, respectively.

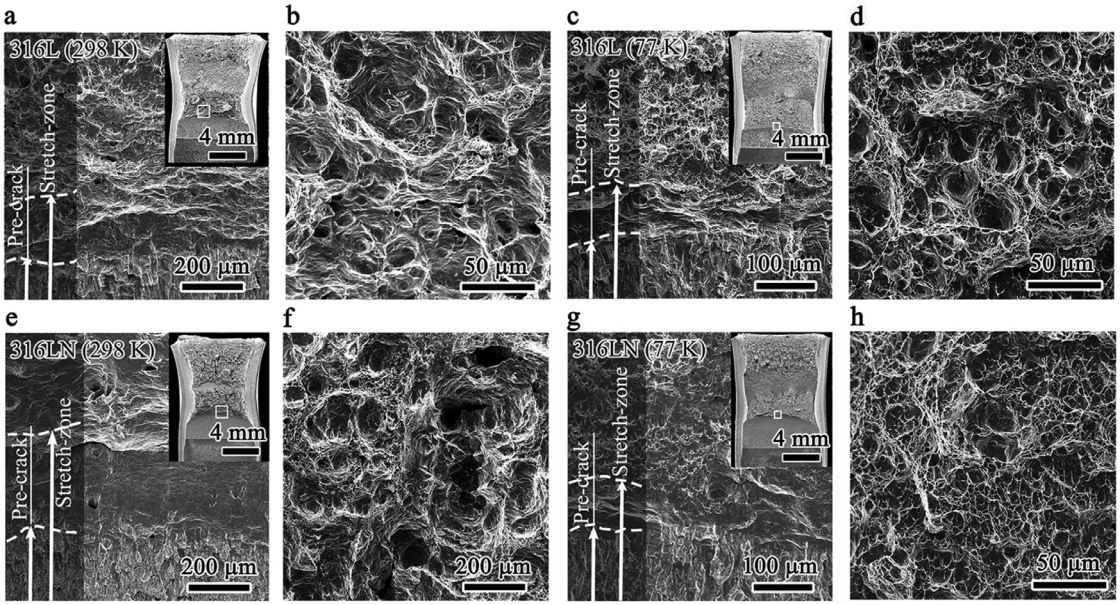

Fig. 13. Fractography after fracture toughness testing in 316L and 316LN. (a) The transition zone from the pre-crack to a pronounced stretch-zone of 316L at 298 K. Insert is a comprehensive outline of the fracture surface. Pre-crack boundary and stretch-zone boundary are marked by the dashed line on the left shaded area of (a). (b) Fracture surface in crack growth region in 316L at 298 K. (c) Transition zone from the pre-crack to a pronounced stretch-zone of 316L at 77 K. (d) Fracture surface at crack growth region of 316L at 77 K. (e) and (f) Transition zone and fracture surface in crack growth region in 316LN at 298 K, respectively. (g) and (h) Transition zone and fracture surface in crack growth region in 316LN at 77 K, respectively.

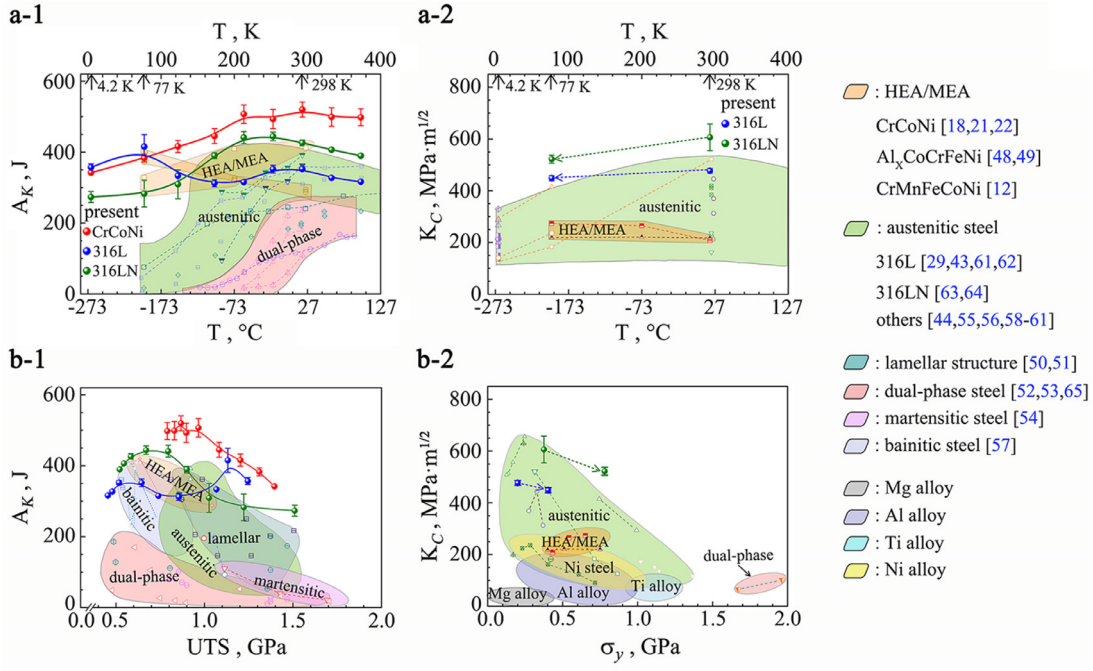

Fig. 14. Strength-toughness balance. (a-1) and (a-2) A_K and K_C vs temperature (T), respectively. (b-1) and (b-2) (A_K, UTS) balance and (K_C, σ_y) balance. A_K: Charpy impact energy. K_C: fracture toughness. σ_y: yield strength. UTS: ultimate tensile strength. Dotted arrows show the trend with decreasing temperature from 298 K to 77 K.

atoms in alloys will increase the stability of austenite [34,46,47], so transformation to α' cannot play an important role as that in 316L.

The excellent impact toughness of CrCoNi has been reported before [21,22]. It was explained that the primary NTs induced inherent toughening *via* significant strain hardening, and secondary twinning exhibited a special advantage of targeted blockage of SB propagation and delayed the transition from SB to crack, inhibiting the rapid and unstable propagation of cracks. This mechanism works from 293 K to 77 K, leading to a high A_K over a wide temperature range (373 K to 4.2 K). In comparison, such profuse DTs are far less significant in 316L and 316LN, especially at 77 K. As a result, CrCoNi performs better in dynamic impact deformation.

4.2.3. Hardening mechanism transition with decreasing temperature upon fracture toughness testing

The microstructure evolution after fracture toughness testing is similar to that after impact with decreasing temperature. At 298 K, SBs are generated at the pre-crack tip, along with the formation of dislocations and DTs of high density dynamically ahead of the propagation of SBs in 316L (Fig. 10(b) and (c)). The dislocation ac-

tivities and DTs provide the main hardening mechanisms at 298 K in 316L. Meanwhile, obvious passivation of crack tip (Fig. 10(a) and Fig. 13(a)) is related to strong strain hardening at the crack tip. At 77 K, α'-martensite transformation occurs along the path of crack growth. The α' inside grains and SBs provides strain hardening in the plastic zone of the crack tip. Furthermore, r_c decreases with temperature drops in 316L (Fig. 5(c)), leading to the decrease of K_C.

In 316 LN, high-density dislocations and DTs are the dominant plastic mechanism at the crack tip at 298 K (Fig. 11(b) and (c)). The blunting of the crack tip is more severe than that in 316L at 298 K, according to the size of the stretch-zone (Fig. 13(a) and (e)). It indicates a stronger hardening behavior at the tip of crack in 316LN. When it drops to 77 K, dislocations, DTs, and α' occur (Fig. 11(e) and (f)). Some martensite assists the deformation near the crack, along with the decrease of r_c (Fig. 5(c)), and K_C drops in 316LN, as well, compared with that at 298 K. In addition, V_{FCC} is 86% near crack after fracture in 316LN, which is much higher than that in 316L (V_{FCC} ~57%). Hence, it shows a higher K_C in 316LN than that in 316L at 77 K (Fig. 14(a-2)), due to a lower toughness of α'-martensite than austenite [44].

It has been reported that the fracture toughness in CrCoNi increased with decreasing temperature from 293 K to 77 K [18]. DTs were activated at 293 K, but increased so much that they played an even more prominent role when the temperature dropped to 77 K [18]. Therefore, K_C of CrCoNi increases with the decrease of temperature, while K_C of 316L and 316LN decreases. That is to say, CrCoNi becomes better with decreasing temperature, consistent with a more excellent strength-ductility combination of CrCoNi than 316L and 316LN at low temperatures.

4.3. Influence of strain rate on toughness

The strain rate for quasi-static fracture toughness (~10^{-4} s^{-1}) differs from that in dynamic impact test (~10^{3} s^{-1}) by seven orders of magnitude. At high strain rate impact, DTs with thickness and spacing of only a few nanometers are formed in CrCoNi [22].

The mechanism of strain hardening in 316L at the crack tip is similar to that in the impact testing. Work hardening is provided by dislocation activities and NTs at 298 K and TRIP mechanism at 77 K (Figs. 6 and 7). There are, however, two notable differences in the crack propagation pattern: (1) Upon impact loading, the main crack is passivated, and secondary cracks develop and converge with microcracks (narrow width: 20 μm, in Fig. 8(b)) in 316 L at 298 K, while at crack tip upon fracture toughness testing at 298 K, only the primary crack propagates. The micro-void is elliptical with a width of 150 μm, as shown in Fig. 10(a). The difference in crack propagation pattern is probably related to the stress state experienced by the samples, and the complicated stress state in dynamic impact may promote the development of secondary cracks. C(T) samples have a larger void than CVN sample at the same testing temperature, and this also can be seen by comparing the size of the dimples after impact (Fig. 12) with those after fracture (Fig. 13). That is to say, the toughness decreases with increasing strain rate. (2) With the increase of strain rate, DTs become more popular at 298 K (Fig. 8(b) and Fig. 9(b)) and α' is reduced at 77 K (Table 2), compared with that under quasi-static loading in 316L (Fig. 10(b)) and 316LN (Fig. 11(c)). This is because a raised flow stress makes it easier to reach the critical stress for twining under dynamic loading [24,66]. The measured V_{FCC} after impact is much higher than that after tensile and fracture toughness testing at a given temperature (Table 2), which is similar to the observation in VCrFeCoNi [67]. This was explained as due to the rise of temperature during dynamic loading, resulting in an increase in $\Delta G^{FCC\rightarrow BCC}$ (difference in Gibbs free energy between BCC and FCC phases) [67]. As a result, phase transformation from γ to α' becomes difficult under the dynamic loading.

5. Conclusions

The tensile, impact and fracture toughness properties of CrCoNi in comparison with 316L and 316LN were investigated, and several conclusions can be drawn from this work, in regards to the properties at various temperatures and associated mechanisms:

(1) In terms of tensile properties, the three FCC alloys are similar at 298 K, while CrCoNi shows a particularly impressive strength-plasticity synergy at 4.2 K. The austenite of CrCoNi is stable even at 4.2 K, with nanoscale deformation twinning dominating to provide a high work-hardening capability. In 316L, at cryogenic temperature, martensitic transformation becomes the main deformation mechanism together with dislocation activities. In 316LN, DTs, limited α' martensite and dislocation activities carry the deformation at 77 K and 4.2 K.

(2) In Charpy impact testing, CrCoNi has a remarkable Charpy impact energy (A_K) compared to 316L and 316LN, especially at 4.2 K, as nanoscale deformation twinning blocks the propagation of SBs and provides hardening in SBs. There is an abnormal rebound of A_K in 316L at about 200 K, as profuse α' ahead of crack tip delocalize the strain. In 316LN, deformation twinning assists dislocation activities to carry plastic deformation at 298 K, while some martensitic transformations occur at cryogenic temperatures.

(3) In fracture toughness testing, the K_{JIC} of CrCoNi increases with decreasing test temperature, due to the increase of the density of deformation twins. By contrast, in 316L and 316LN, K_C decreases moderately with decreasing temperature. However, the stainless steels appear to have better toughness than the CrCoNi at all temperatures. The deformation mechanism changes from nano-twining to martensitic transformation in 316L from 298 K to 77 K. As for 316LN, dislocation activities dominate work-hardening at both 298 K and 77 K, with the assistance from DTs at 298 K and from DTs and limited martensitic transformation (as austenite is stabilized by nitrogen) at 77 K.

All in all, these three alloys share many traits in common. The comparison made in this work justifies the proposition to expand the realm of FCC MEAs. Specifically, we advocate to include the previously well-known austenitic stainless steels as MEAs. These alloys all start out as concentrated single-phase FCC solid solutions based on 3d transition metals, such that we can rightfully categorize them simply as next-of-kin sub-groups of MEAs. Their mechanical performances are comparable, in terms of tensile, impact and toughness properties, which are similarly impressive (and particularly so as cryogenic alloys). Their excellent properties are a rationale to reinforce the notion that the MEAs are special, with major societal impact. These alloys all rely heavily on shear transformations in plastic deformation, with deformation twinning dominant in CrCoNi, and martensitic transformation involved in the stainless steels. There are nevertheless interesting differences in terms of the temperature dependence of the magnitude of the properties, suggesting the need for more in-depth studies of the underlying mechanisms and their temperature dependence.

Acknowledgments

This work was financially supported by the Ministry of Science and Technology of China (Grant Nos. 2019YFA0209900 and 2017YFA0204402), the NSFC Basic Science Center Program for "Multiscale Problems in Nonlinear Mechanics" (Grant No.

11988102), the NSFC (Grant Nos. 11972350 and 11890680), and the Strategic Priority Research Program of the Chinese Academy of Sciences (Grant No. XDB22040503). E. Ma acknowledges XJTU for hosting his research at CAID.

Supplementary materials

Supplementary material associated with this article can be found, in the online version, at doi:10.1016/j.jmst.2021.08.057.

References

[1] M.H. Tsai, J.W. Yeh, Mater. Res. Lett. 2 (2014) 107–123.
[2] Y.F. Ye, Q. Wang, J. Lu, C.T. Liu, Y. Yang, Mater. Today 19 (2016) 349–362.
[3] D.B. Miracle, O.N. Senkov, Acta Mater. 122 (2017) 448–511.
[4] S. Wei, F. He, C.C. Tasan, J. Mater. Res. 33 (2018) 2924–2937.
[5] E.P. George, D. Raabe, R.O. Ritchie, Nat. Rev. Mater. 4 (2019) 515–534.
[6] E. Ma, X.L. Wu, Nat. Commun. 10 (2019) 5623.
[7] E.P. George, W.A. Curtin, C.C. Tasan, Acta Mater. 188 (2020) 435–474.
[8] Z. Wu, H. Bei, F. Otto, G. Pharr, E.P. George, Intermetallics 46 (2014) 131–140.
[9] Z. Wu, H. Bei, G.M. Pharr, E.P. George, Acta Mater. 81 (2014) 428–441.
[10] E. Ma, Scr. Mater. 181 (2020) 127–133.
[11] F. Otto, A. Dlouhy, C. Somsen, H. Bei, G. Eggeler, E.P. George, Acta Mater. 61 (2013) 5743–5755.
[12] B. Gludovatz, A. Hohenwarter, D. Catoor, E.H. Chang, E.P. George, R.O. Ritchie, Science 345 (2014) 1153–1158.
[13] Z.J. Zhang, M.M. Mao, J.W. Wang, B. Gludovatz, Z. Zhang, S.X. Mao, E.P. George, Q. Yu, R.O. Ritchie, Nat. Commun. 6 (2015) 10143.
[14] Y. Deng, C.C. Tasan, K.G. Pradeep, H. Springer, A. Kostka, D. Raabe, Acta Mater. 94 (2015) 124–133.
[15] M. Kawamura, M. Asakura, N.L. Okamoto, K. Kishida, H. Inui, E.P. George, Acta Mater. 203 (2021) 116454.
[16] J. Mao, C.E. Slone, T.M. Smith, C. Niu, H. Bei, M. Ghazisaeidi, G.M. Pharr, M.J. Mill, Acta Mater. 132 (2017) 35–48.
[17] Z.J. Zhang, H.W. Sheng, Z.J. Wang, B. Gludovatz, Z. Zhang, E.P. George, Q. Yu, S.X. Mao, R.O. Ritchie, Nat. Commun. 8 (2017) 14390.
[18] B. Gludovatz, A. Hohenwarter, K.V.S. Thurston, H.B. Bei, Z.G. Wu, E.P. George, R.O. Ritchie, Nat. Commun. 7 (2016) 10602.
[19] M.X. Yang, D.S. Yan, F.P. Yuan, P. Jiang, E. Ma, X.L. Wu, Proc. Natl. Acad. Sci. U.S.A. 115 (2018) 7224–7229.
[20] Y. Ma, F.P. Yuan, M.X. Yang, P. Jiang, E. Ma, X.L. Wu, Acta Mater. 148 (2018) 407–418.
[21] M.X. Yang, L.L. Zhou, C. Wang, P. Jiang, F.P. Yuan, E. Ma, X.L. Wu, Scr. Mater. 172 (2019) 66–71.
[22] X.L. Wu, M.X. Yang, P. Jiang, C. Wang, L.L. Zhou, F.P. Yuan, E. Ma, Scr. Mater. 178 (2020) 452–456.
[23] A. Gali, E.P. George, Intermetallics 39 (2013) 74–78.
[24] G. Laplanche, A. Kostka, C. Reinhart, J. Hunfeld, G. Eggeler, E.P. George, Acta Mater. 128 (2017) 292–303.
[25] Q.Q. Ding, X.Q. Fu, D. Chen, H.B. Bei, B. Gludovatz, J.X. Li, Z. Zhang, E.P. George, Q. Yu, T. Zhu, R.O. Ritchie, Mater. Today 25 (2019) 21–27.
[26] B. Fultz, A. DuBois, H.J. Kim, J.W.M. Jr, Cryogenics 24 (1984) 687–690.
[27] K.H. Lo, C.H. Shek, J.K.L. Lai, Mater. Sci. Eng. R 65 (2009) 39–104.
[28] T.S. Desisto, Tech. Rep. (1963).
[29] W.J. Mills, Int. Mater. Rev. 42 (1997) 45–82.
[30] X.L. Wu, M.X. Yang, F.P. Yuan, L. Chen, Y.T. Zhu, Acta Mater. 112 (2016) 337–346.
[31] Y. Ma, M.X. Yang, P. Jiang, F.P. Yuan, X.L. Wu, Sci. Rep. 7 (2017) 15619.
[32] E23-18 Standard Test Method for Notched Bar Impact Testing of Metallic Materials, ASTM International, 2018.
[33] E1820-18 Standard Test Method for Measurement of Fracture Toughness, ASTM International, 2018.
[34] M.L.G. Byrnes, M. Grujicic, W.S. Owen, Acta Metall. 35 (1986) 1853–1862.
[35] Y. Han, H.B. Li, H. Feng, Y.Z. Tian, Z.H. Jiang, T. He, Mater. Sci. Eng. A 814 (2021) 141235.
[36] S.Y. Chen, X. Xie, W.D. Li, R. Feng, B.L. Chen, J.W. Qiao, Y. Ren, Y. Zhang, K.A. Dahmen, P.K. Liaw, Mater. Chem. Phys. 210 (2018) 20–28.
[37] D.W. Kim, W.S. Ryu, J.H. Hong, J. Mater. Sci. 33 (1998) 675–679.
[38] V. Seetharaman, R. Krshnan, J. Mater. Sci. 16 (1981) 523–530.
[39] T.S. Byun, N. Hashimoto, K. Farrell, Acta Mater. 52 (2004) 3889–3899.
[40] R. Chaouadi, A. Fabry, Eur. Struct. Integr. Soc. 30 (2002) 103–117.
[41] B. Hwang, T.H. Lee, S.J. Park, C.S. Oh, S.J. Kim, Mater. Sci. Eng. A 528 (2011) 7257–7266.
[42] H. Kim, J. Park, J.E. Jung, S.S. Sohn, S. Lee, Mater. Sci. Eng. A 641 (2015) 340–347.
[43] A.J. Cooper, N.I. Cooper, A. Bell, J. Dhers, A.H. Sherry, Metall. Mater. Trans. A 46 (2015) 5126–5138.
[44] M.X. Zhang, P.M. Kelly, J. Mater. Sci. 37 (2002) 3603–3613.
[45] H.O. Fuchs, R.I. Stephens, Metal fatigue in engineering, John Wiley & Sons Inc., New York, 1980.
[46] M. Grujicic, W.S. Owen, Acta Metall. Mater. 43 (1995) 4201–4211.
[47] I. Karaman, H. Sehitoglu, H.J. Maier, Y.I. Chumlyakov, Acta Mater. 49 (2001) 3919–3933.
[48] S.Q. Xia, M.C. Gao, Y. Zhang, Mater. Chem. Phys. 210 (2018) 213–221.
[49] D.Y. Li, Y. Zhang, Intermetallics 70 (2016) 24–28.
[50] W.Q. Cao, M.D. Zhang, C.X. Huang, S.Y. Xiao, H. Dong, Y.Q. Weng, Sci. Rep. 7 (2017) 41459.
[51] M.D. Zhang, H. Xu, W.Q. Cao, H. Dong, ISIJ Int. 56 (2016) 861–867.
[52] C.N. Li, Y. Guo, F.Q. Ji, D.S. Ren, G.D. Wang, Mater. Sci. Eng. A 665 (2016) 98–107.
[53] Y.J. Chao, J.D.W. Jr, R.G. Sands, Mater. Des. 28 (2007) 551–557.
[54] H. Kim, J. Park, M. Kang, S. Lee, Mater. Sci. Eng. A 649 (2016) 57–67.
[55] M. Milititsky, D.K. Matlock, A. Regully, N. Dewispelaere, J. Penning, H. Hanninen, Mater. Sci. Eng. A 496 (2008) 189–199.
[56] B. Hwang, T.H. Lee, S.J. Kim, Met. Mater. Int. 16 (2010) 905–911.
[57] Y.R. Im, J.O. Yong, B.J. Lee, J.H. Hong, H.C. Lee, J. Nucl. Mater. 297 (2001) 138–148.
[58] K.G. Samuel, O. Gossmann, H. Huthmann, Int. J. Pres. Ves. Pip. 41 (1990) 59–74.
[59] D.T. Read, R.P. Read, Cryogenics 21 (1981) 415–417.
[60] P. Deimel, H. Fischer, M. Hoffmann, J. Mater. Sci. 33 (1998) 1105–1116.
[61] J.E. Pawel, D.J. Alexander, M.L. Grossbeck, A.W. Longest, A.F. Rowcliffe, G.E. Lucas, S. Jitsukawa, A. Hishinuma, K. Shiba, J. Nucl. Mater. 212-215 (1994) 442–447.
[62] L. Xiong, Z.S. You, S.D. Qu, L. Lu, Acta Mater. 119 (2016) 55–59.
[63] B.S. Dutt, G. Shanthi, G. Sasikala, M.N. Babu, S. Venugopal, S.K. Albert, A.K. Bhaduri, T. Jayakumar, Procedia Eng 86 (2014) 302–307.
[64] G. Sasikala, S.K. Ray, J. Nucl. Mater. 408 (2011) 45–53.
[65] L. Liu, Q. Yu, Z. Wang, J. Ell, M.X. Huang, R.O. Ritchie, Science 368 (2020) 1347–1352.
[66] J. Park, M. Kang, S.S. Sohn, S.H. Kim, H.S. Kim, N.J. Kim, S. Lee, Mater. Sci. Eng. A 684 (2017) 54–63.
[67] Y.H. Jo, D.G. Kim, M.C. Jo, K.Y. Doh, S.S. Sohn, D. Lee, H.S. Kim, B.J. Lee, S. Lee, J. Alloys Compd. 785 (2019) 1056–1067.